Determining fast-S and slow-S propagation directions with SV-P data produced by buried explosives and recorded with vertical geophones

Bob Hardage[1], Mike Graul[2], Tim Hall[2], Chris Hall[2], Mark Kelley[3], Valerie Smith[3], and Allen Modroo[4]

Abstract

We have evaluated the concept of practicing S-wave reflection seismology with legacy 3D seismic data generated by a P-wave source and recorded with only vertical geophones. This type of S-wave imaging is based on the principle that seismic P-wave sources not only produce a downgoing illuminating P wavefield, but they also simultaneously produce a downgoing illuminating SV wavefield that, in almost all cases, is suitable for S-wave reflection imaging. The S-mode used in this study is the SV-P, or converted-P, mode. This mode involves a downgoing illuminating SV wavefield and an upgoing reflected P-mode that is recorded by vertical geophones. In flat-layered stratigraphy, the lengths of the SV and P raypaths in SV-P imaging are identical to the lengths of the SV and P raypaths in P-SV imaging with P-sources and 3C geophones. P-SV imaging of deep rocks has been practiced for more than two decades; SV-P imaging is a new concept. SV-P data should provide the same options for investigating deep rocks as do P-SV data. We have determined one of the equivalences between SV-P data extracted from vertical-geophone data and P-SV data extracted from horizontal geophones: that both modes react to azimuth-dependent variations in the S velocity in anisotropic rocks. Azimuthal variations in the SV-P traveltime can be used to define the polarization direction of the fast-S-wave mode, which is also the azimuth of the maximum horizontal stress (SHmax). Our investigation demonstrates a noninvasive method for monitoring changes in the SHmax azimuth across a CO_2 storage reservoir, or any targeted porous rock, as fluids are cycled into, and then out of, that rock's pore space.

DOI:10.1190/INT-2020-0226.1

Introduction

The specific S-mode used in this 3D seismic study is the SV-P mode, which is a seismic imaging option that seems to have been ignored by geophysicists. An SV-P mode involves a downgoing, direct-S, illuminating wavefield produced by a P-source and upgoing P reflections generated by that downgoing S wavefield by SV-to-P mode conversions at deep rock interfaces. These mode-converted, upgoing, P reflections are recorded by surface-based vertical geophones, just as upgoing P reflections that are generated by a downgoing, illuminating P wavefield are recorded. An alternate terminology that could be used for the SV-P mode would be to refer to SV-P data as a converted-P mode. This terminology is consistent with the term converted-S that has been adopted to refer to the P-SV mode generated by P-sources and recorded by horizontal geophones.

The fact that SV-P reflections are recorded by surface-based vertical geophones means that thousands of square miles of legacy 3D vertical-geophone data that are already preserved in digital data libraries can be retrieved and reprocessed for SV-P imaging when S-wave information is needed. In fact, legacy vertical-geophone data recorded in 2008 were retrieved from storage and reprocessed to generate the SV-P data illustrated in this paper.

Anisotropic rocks

Stiffness coefficients in an *anisotropic* rock differ when they are measured in different azimuth directions. A simple, but commonly used, model for describing anisotropic rock is illustrated in Figure 1. This model shows a system of vertical, aligned, extensional fractures and the azimuths of the SHmax and SHmin horizontal stresses associated with those fractures. Although this model does not allow shear fractures, which are aligned at angles of approximately 30° relative to extensional fractures, it is still an adequate model for our purposes. The vertical plane that is oriented in the direction of aligned, extensional fractures (SHmax azimuth) is the *isotropy plane*, and the vertical plane perpendicular to

[1]Consultant, Maumee, Ohio 43537, USA. E-mail: bob.hardage@utexas.edu (corresponding author).
[2]Texseis, Houston, Texas 77055, USA. E-mail: mgraul@texseis.com; thall@texseis.com; chall@texseis.com.
[3]Battelle, Columbus, Ohio 43201, USA. E-mail: kelleym@battelle.org; smithvl@battelle.org.
[4]CORE Energy, Traverse City, Michigan 49684, USA. E-mail: amodroo@coreenergyllc.com.

Manuscript received by the Editor 24 November 2020; published ahead of production 6 February 2021; published online 22 April 2021. This paper appears in *Interpretation*, Vol. 9, No. 2 (May 2021); p. T599–T609, 13 FIGS.
http://dx.doi.org/10.1190/INT-2020-0226.1.

the aligned fractures (SHmin azimuth) is the *symmetry plane*.

A seismic wavelet that propagates through anisotropic rock exhibits a unique characteristic in that its propagation velocity depends on the horizontal angle between the orientation of the wavelet's displacement vector and the direction in which the isotropy plane (SHmax azimuth) is oriented. Laboratory studies by Xu and King (1989) and P-wave velocity analyses and imaging by Al-Hawas et al. (2003), Lynn (2004a, 2004b), and Smith and McGarrity (2001) show that the velocities of P-waves that travel through anisotropic rock in a direction that parallels the isotropy plane are slightly faster than the velocities of P-waves that propagate in the direction of the symmetry plane. In contrast, S-wave velocities in these two orthogonal directions can differ significantly. Thus, if investigators have the option of using either P-wave data or S-wave data to determine the azimuth of SHmax in an anisotropic rock, most investigators will opt to use S-wave data. In our SHmax study, we had the option of using either P-P data or SV-P data. We found that SV-P data provided more reliable estimates of SHmax than did P-P data.

Recognizing P-P and SV-P reflections in trace gathers

P-P reflections and SV-P reflections are intertwined in trace gathers of vertical-geophone data. To use SV-P data, it is necessary to recognize the differences in the SV-P and P-P reflections in prestack data so that wavefield separation procedures can be implemented that will segregate the SV-P and P-P reflections into separate data-processing streams. A real-data example illustrating how P-P and SV-P reflection events are entangled with each other in a P-P trace gather of vertical-geophone data is shown in Figure 2. These data were acquired in a previous study and are used here because of the high quality of the two independent sets of reflections in that earlier study. The energy source used in that previous study was a buried explosive, similar to the buried-explosive sources that generated the vertical-geophone data that are used in this paper.

The data in Figure 2 are shown as a common-depth-point (CDP) trace gather after performing only one prestack time migration (PSTM) procedure. The flattened reflections that extend across the trace gather are P-P reflections, which are positioned at the same image time for all of the source-to-receiver offsets after this data-migration step. Each P-P reflection appears at the same image time across all of the vertical-geophone trace gather because an accurate P-P migration velocity was used. All P-P traces in this display are located at the same CDP spatial coordinates in the subsurface; the traces have not yet been summed to create that single image trace at those CDP image coordinates.

The curved events that appear in this same vertical-geophone trace gather are SV-P reflections. These SV-P reflections have not been corrected to flat events by the P-P migration velocity because SV-P velocities are slower than P-P velocities. Traditionally, P-P data processors have assumed that these slower velocity events are interbed P-P multiples created at shallower depths. Such interbed multiples would also have a slower velocity than P-P primary reflections. However, researchers at the University of Texas at Austin demonstrated that these ubiquitous events are SV-P converted-mode reflections, and only rarely are interbed multiples. This finding is a significant observation that allows S-wave reflection seismology to be practiced with data created by P-sources and recorded by a vertical geophone

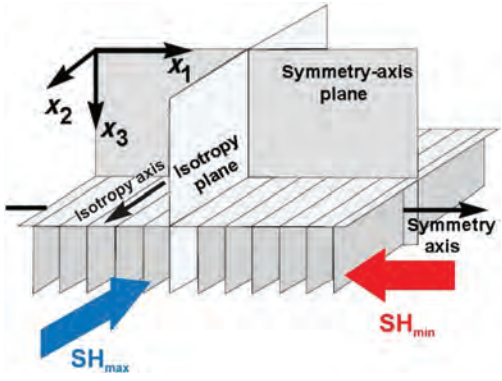

Figure 1. Horizontal transverse isotropy type of anisotropic rock medium and the terminology commonly used to describe seismic wave propagation in such a medium. The principles that are illustrated are (1) as an S-wave travels through an anisotropic medium, it segregates into two daughter S-waves (S1 and S2) that travel with different velocities, (2) the fast-S-mode (S1) is polarized in the same direction as the SHmax azimuth, and (3) the slow-S-mode (S2) is polarized in the same direction as the SHmin azimuth.

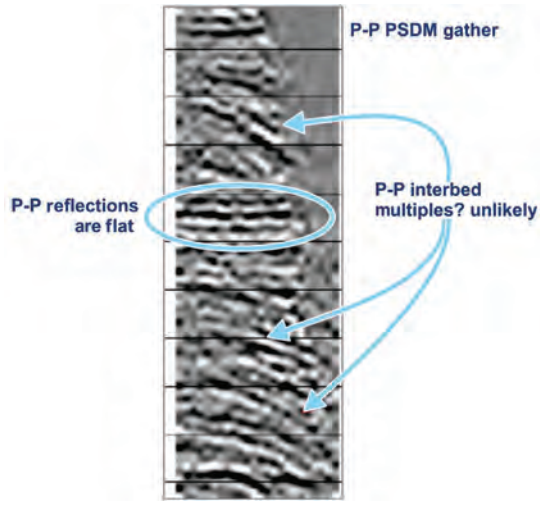

Figure 2. The P-P, CDP, vertical-geophone data after one application of the P-P migration velocities. P-P reflections are flat, as they should be. The down-curving reflections are slower velocity SV-P reflections that are embedded in the same vertical-geophone data. This real-data trace gather is an excellent example of the manner in which P-source P-P reflections and SV-P reflections are entangled in vertical-geophone data. From Graul (2017).

DOI:10.1190/INT-2020-0226.1

(Hardage, 2011, 2012a, 2012b, 2017a, 2017b, 2017c, 2017d; Hardage and Wagner, 2014a, 2014b, 2018a, 2018b; Hardage et al., 2014; Li and Hardage, 2015; Graul, 2017; Gupta and Hardage, 2017; Karr, 2017; Li et al., 2017; Wagner and Hardage, 2017).

Separating the P-P and SV-P wavefields

Model data are used in Figure 3a–3c to illustrate how SV-P reflections in a vertical-geophone trace gather can be suppressed and coherent P-P reflections can be emphasized. Figure 3d–3f then illustrates the same methodology, but now SV-P reflections are flattened (Figure 3e) because the data are migrated with the slower, correct, converted-wave velocity. P-P reflections now curve upward because they have faster velocities than SV-P velocities (Figure 3e). An iterative subtraction process then suppresses the P-P reflections and enhances the SV-P reflections, which are now flattened by migration that uses the correct converted-wave velocity. The end result is wavefield separation, with Figure 3c showing the P-P wavefield, and Figure 3f showing the SV-P wavefield. Both wavefields coexisted in the raw vertical-geophone data (Figure 3a and 3d).

A real-data example of intertwined P-P and SV-P reflections in a P-source, vertical-geophone, trace gather is illustrated in Figure 4. Figure 4a shows a PSDM depth migration of vertical-geophone data, constructed with real P-P velocities, at a stacking bin in a real, P-P 3D image space. P-P reflections are flat, as they should be. The buried explosive source used in this 3D survey created robust downgoing SV illumination wavefields. Obvious, down-curving, SV-P reflections are intermingled with the flattened P-P reflections in this P-P migration of vertical geophone data. Figure 4b shows the same data after an iterative subtraction process is implemented to remove the curved SV-P reflections and expose the pure P-P reflections. These data are an excellent real-data example of the mixing of P-P and SV-P reflections in data generated by a P-source and recorded with only vertical geophones. This intermingling of P-P and SV-P reflections occurs repeatedly in vertical-geophone data in basin after basin where we have done SV-P studies. Research teams have now observed this dual-wavefield behavior in 10 different basins when data are generated by either vertical vibrators or by shot-hole explosives and then recorded by vertical geophones.

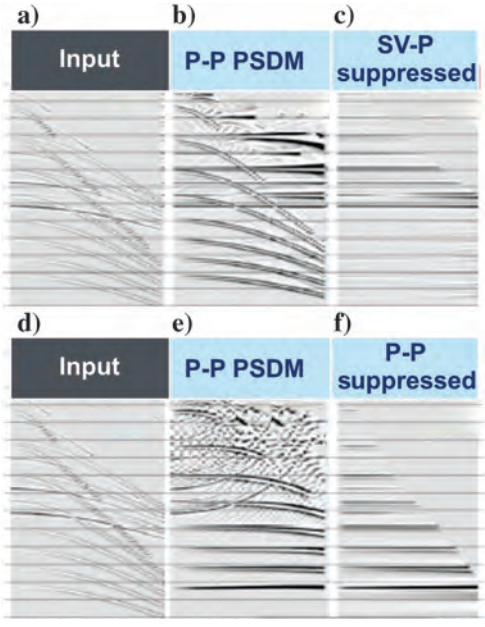

Figure 3. Model-calculated trace gather of P-source vertical-geophone data (a and d). (b) P-P velocities have been used to flatten P-P reflections. SV-P reflections still curve downward. (c) The result of applying filters that suppress curved events, enhance flat events, and leave a high-quality P-P reflection gather. (e) The effects of applying SV-P velocity corrections that flatten SV-P reflections and overcorrect P-P reflections. (f) The SV-P reflections after curved P-P reflections are suppressed. From Graul (2017).

Rotating azimuth sectors

The rotating, narrow-azimuth-corridor strategy that we used to detect the SHmax and SHmin azimuths with SV-P data is illustrated in Figure 5. In this figure, source lines are oriented north–south and source stations are shown as red X marks. Receiver lines are oriented east–west, and vertical-geophone receiver stations are shown in the solid yellow circles. In this example, source stations are shown only on the left side of the stacking bin and receiver stations are shown only on the right side. In practice, source stations on the right side of a stacking bin and receiver stations on the left side also contribute to trace gathers constructed inside an azimuth corridor. All source-receiver pairs inside this example corridor contribute to the SV-P trace gather constructed at stacking bin SB.

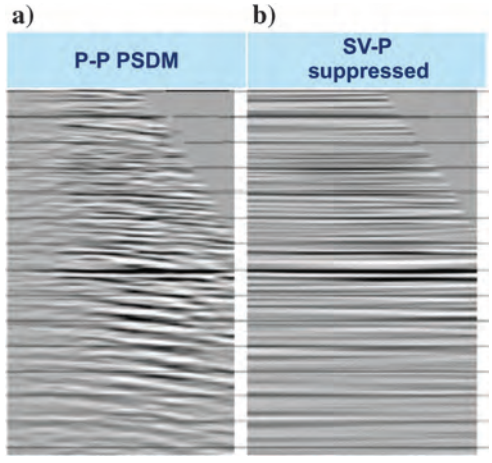

Figure 4. (a) A real P-P trace gather at a stacking bin that has been subjected to a PSDM migration using P-P velocities. The P-P reflections are flat, as they should be. Robust SV-P reflections were also produced by the P-source (buried explosives in this case), and these SV-P reflections appear as down-curving reflections. (b) The P-P trace gather after the curved SV-P reflections are removed by a wavefield subtraction procedure. Taken from Graul (2017).

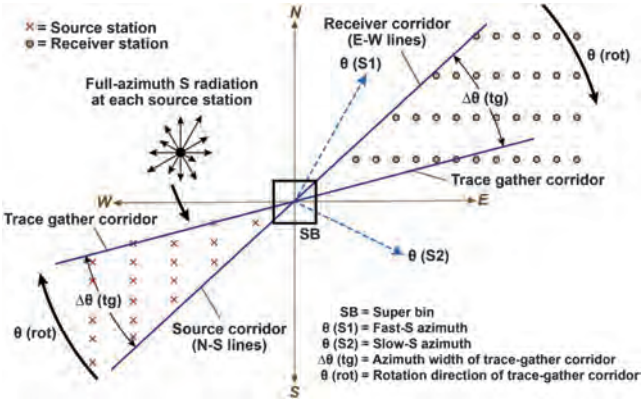

Figure 5. Strategy used to create prestack SV-P trace gathers in narrow rotating azimuth corridors that can define the fast-S and slow-S polarization azimuths. The fast-S azimuth will also be the azimuth of SHmax. The area spanned by the stacking area labeled SB can be a single stacking bin or a superbin spanning an area of several normal-size stacking bins.

A vertical view of a typical, full-azimuth, direct-SV radiation pattern that is produced at a P-source station is shown as a spoke-wheel pattern of black arrows positioned a short distance northwest of stacking bin **SB.** The length of each outward-pointing arrow indicates the magnitude of direct-S displacement that travels away from a P-source station in the direction of that arrow. This full azimuth of the takeoff-angle directions of direct-SV radiation from a P-source station ensures that every azimuth corridor around a P-source station will be illuminated with downgoing SV energy.

The length of the SV displacement vector in this spoke-wheel radiation pattern varies with azimuth depending on how the stiffness coefficients immediately around a source station vary with azimuth. For example, features that affect stiffness coefficients around a vertical-vibrator baseplate can be benign conditions such as deep-rooted vegetation on one side of a vibrator baseplate but shallow-rooted vegetation on the other side, a field vehicle or a second vibrator positioned

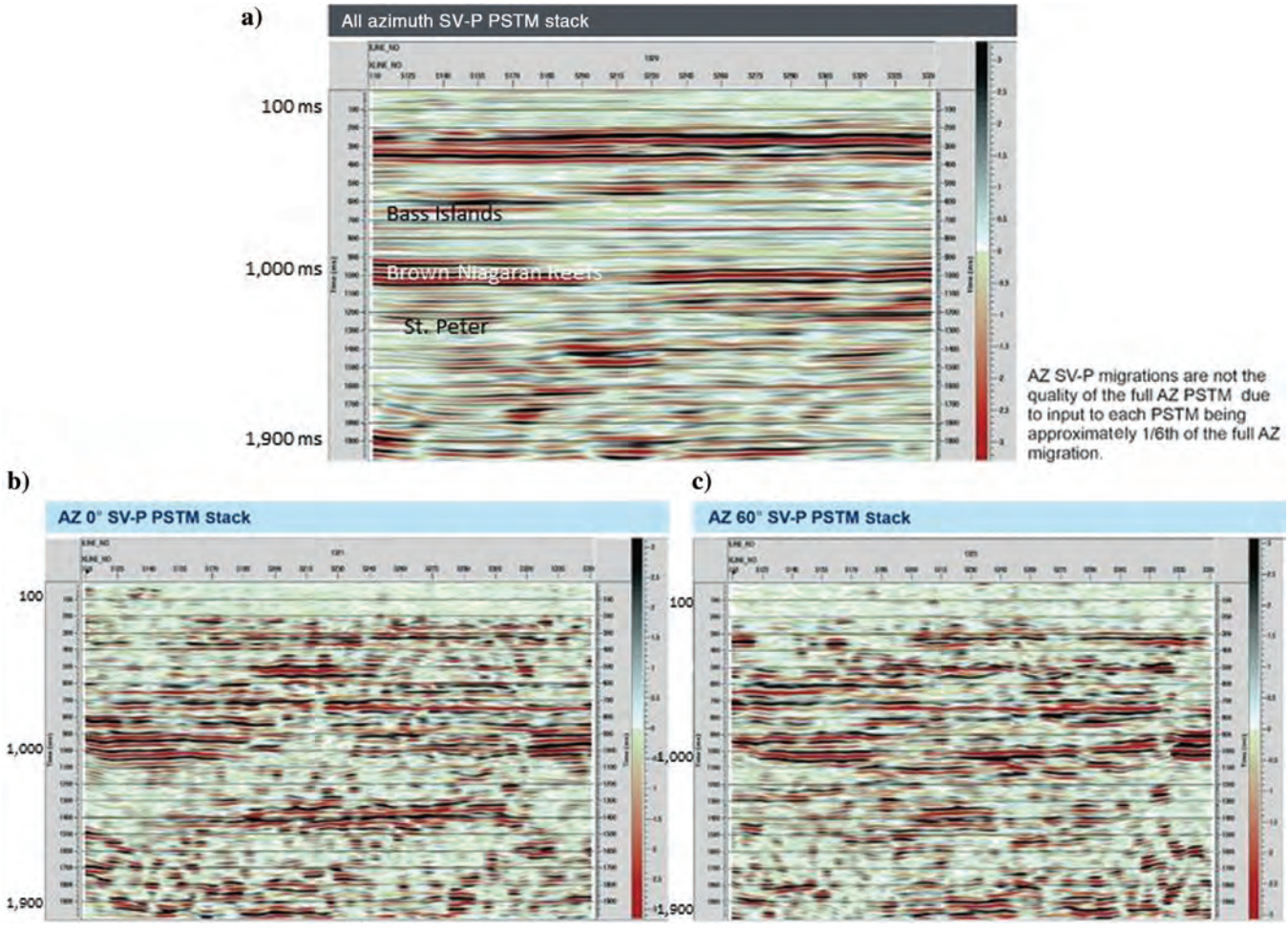

Figure 6. (a) Inline 1320 from the SV-P 3D volume after the data have been imaged using a full-azimuth PSTM procedure. A designation preferred by many for the reflections labeled Brown Niagaran Reefs is *A2 carbonate.* (b) Inline 1320 using a PSTM procedure limited to sources and receivers positioned inside a 30°-wide azimuth corridor that is oriented from 0° to 180° (north to south). (c) Inline 1320 using a PSTM procedure limited to sources and receivers positioned inside a 30°-wide azimuth corridor that is oriented from 60° to 240° (east–northeast to west–southwest).

beside an active vibrator, and unseen variations in the mineralogy mixture and porosity of the surface layer and near-surface layers. Finite-difference modeling demonstrates how a small-scale, near-source irregularity of this nature causes the takeoff direction of the downgoing SV illumination from a P-source station to move to a near-vertical, and even to a true-vertical, travel direction (Hardage and Wagner, 2018a, 2018b). These true-vertical and near-vertical takeoff directions are essential for proper SV illumination of deep-rock targets.

After the stacking-bin size and the corridor width are selected, the stacking corridor in Figure 5 is rotated in a clockwise direction around stacking bin SB as shown by arrows labeled θ(rot). An investigator may or may not position adjacent azimuth corridors so that they overlap. Data processors have to experiment to decide how much corridor overlap, if any, should be used.

The fundamental requirement for implementing this rotating-corridor type of SHmax data analysis is to segregate 3D data space into narrow rotating azimuth corridors as illustrated in Figure 5 and then to use a trace-gather data-processing strategy that will illustrate the arrival times of key targeted SV-P reflections inside each of these rotating data corridors. If the earliest-arriving SV-P reflection times occur in a consistent azimuth direction at a significant number of x–y coordinates across the data-acquisition space, it is reasonable to conclude that this earliest-arrival azimuth direction is probably the azimuth of SHmax (i.e., the fast-S direction).

This process will be demonstrated using work by Hardage et al. (2020) who process a 3D seismic survey to estimate SHmax stress azimuths across three horizon depths that spanned an area of approximately 40 mi^2 (approximately 100 km^2). Examples of full-azimuth SV-P images, and SV-P images constructed inside narrow rotating 30°-wide azimuth corridors are exhibited in Figures 6 and 7 for one inline across this 3D image space. The full-azimuth SV-P image displayed in Figures 6a and 7a in each of these figures is reasonable-quality data, even though, as will be demonstrated,

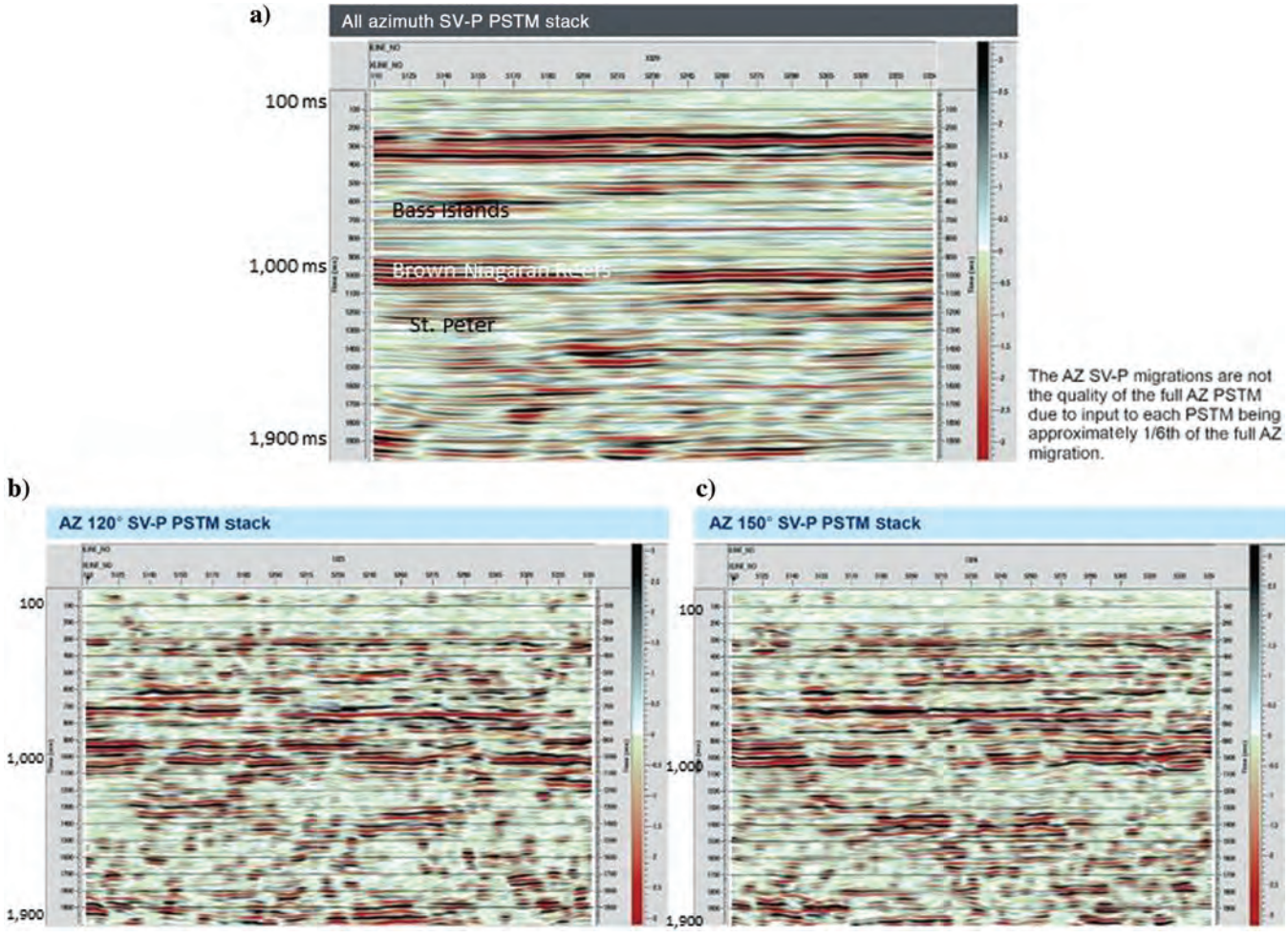

Figure 7. (a) Inline 1320 from the SV-P 3D volume after the data have been imaged using a full-azimuth PSTM procedure. A designation preferred by many for the reflections labeled Brown Niagaran Reefs is *A2 carbonate*. (b) Inline 1320 using a PSTM procedure limited to sources and receivers positioned inside a 30°-wide corridor oriented from 120° to 300° (east–southeast to west–northwest). (c) Inline 1320 using a PSTM procedure limited to sources and receivers positioned inside a 30°-wide corridor oriented from 150° to 330° (south–southeast to north–northwest).

DOI:10.1190/INT-2020-0226.1

SV wavefields in this survey area propagate as fast-S- and slow-S-modes. Thus, this full-fold SV-P image is a sum of fast-S reflections and time-delayed slow-S reflections that interfere with each other and reduce the image quality.

As expected, images made from SV-P narrow-corridor data (Figures 6b, 6c, 7b, and 7c) are of lower quality. There are at least three reasons why the image quality decreases in these narrow-corridor images. First, the size of each stacking bin is only 82.5 × 82.5 ft (25 × 25 m), and the corridor width is only 30°. Thus, only a small number of source-receiver pairs can contribute to a stacking bin inside each rotating narrow-azimuth corridor. The result is a low-fold image. Second, a river flows north–south through the central portion of the image area and reduces the number of available source-receiver pairs in a large number of rotating corridors. Third, full-offset, full-azimuth data cannot be constructed close to the borders of the 3D survey. Even so, significant portions of each narrow 30° wide azimuth corridor shown in Figures 6 and 7 have an acceptable SV-P reflection signal quality.

The azimuth-dependent SV-P traveltime was evaluated at three key stratigraphic horizons — Bass Islands, Brown Niagaran (A2 carbonate), and St. Peter. These horizons are labeled in Figures 6a and 7a. The approximate locations of these targeted horizons are the Bass Islands (approximately 700 ms), Brown Niagaran and A2 carbonate (approximately 1000 ms), and St. Peter (approximately 1200 ms), depending on where the data are examined across this 40 mi^2 (100 km^2) seismic survey. Horizons are not labeled in Figures 6b, 6c, 7b, and 7c so that lower fold reflection events can be better viewed and evaluated.

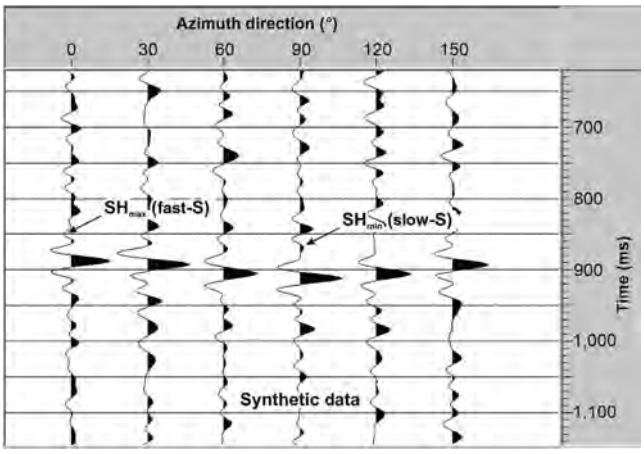

Figure 8. Synthetic SV-P traces calculated for an anisotropic medium like that illustrated in Figure 1. Each trace is an SV-P image trace positioned at the center of a hypothetical image bin. Each trace is created by migrating SV-P reflection traces produced by source-receiver pairs constrained to be inside rotating azimuth corridors that are only 30° wide. The centerline of each corridor is labeled across the top of the display. The positive- and negative-offset portions of these six corridors cover the full 360° of the azimuth compass. Fast-S and slow-S directions in this model are arbitrarily oriented at azimuths of 0° and 90°, respectively.

Procedure for determining the azimuth-dependent SV-P velocities

At each stacking bin, PSTM movements of time samples of SV-P reflections are done inside rotating corridors that are only 30° wide. The positive- and negative-offset portions of six rotating corridors are thus required to capture all source-receiver pairs distributed completely around each stacking bin. The result will be that six migrated SV-P traces will contribute to an SV-P image at each stacking bin. The centerline of the 30° wide corridors that we used were oriented 0°–180°, 30°–210°, 60°–240°, 90°–270°, 120°–300°, and 150°–330° at each stacking bin. Figures 6a and 7a show a full-fold PSTM image along one inline profile across the survey area. Figures 6b, 6c, 7b, and 7c provide four examples of narrow-azimuth-corridor PSTM results along that same inline profile for comparison with the full-fold image. After six narrow-corridor traces are produced at each stacking bin, the next task is to decide which of the six traces in each stacking bin has the earliest SV-P arrival time. The azimuth corridor that contributes the earliest-arriving version of a targeted SV-P reflection should be oriented in the polarization direction of the fast mode of SV-P data. This fast-SVP azimuth will also be the SHmax azimuth at the x–y coordinates of that stacking bin.

The synthetic, model-calculated, SV-P reflection traces in Figure 8 will be used to illustrate the numerical procedure that was used to determine fast-S direction across the 3D survey area that we investigated. Although the earliest-arriving and latest-arriving SV-P wavelets can be recognized by visual inspection, decisions based on visual inspection are not a practical approach to evaluating azimuthal influence on SV-P wavelet arrival times across a 3D data space containing more than 100,000 stacking bins. An efficient and accurate numerical procedure must be developed. Additional challenges that have to be faced when decisions are made by visual inspection are that many SV-P data traces will be contaminated by noise, SV-P reflection wavelets will not have consistent shapes, and accurate arrival times of SV-P reflection wavelets can be difficult to determine.

Thus, a numerically based method has to be implemented to determine the first-arriving SV-P reflection wavelet in each of the approximately 100,000 stacking bins across the SV-P image space that we studied. The method used in this analysis was a crosscorrelation technique. First, a reference SV-P reflection trace is produced at each stacking bin by shifting the azimuth-dependent arrival times of the six reflection wavelets in that bin to a constant arrival time (the left side of Figure 9). These six time-aligned wavelets are then summed to create an improved-quality reference wavelet for that specific image bin (the right side of Figure 9). This time shifting and summing of traces increases the

DOI:10.1190/INT-2020-0226.1

signal-to-noise character of the summed wavelet and simultaneously reduces the random noise portions of the narrow-corridor traces above and below the reflection wavelet.

Then, this new reference trace, with its optimal-quality SV-P reflection wavelet, is crosscorrelated with each of the six original azimuth-dependent traces as shown by the model traces in Figure 10. In this second model-trace analysis in Figure 10, the fast-S azimuth has been repositioned at the 30° azimuth, not at the 0° azimuth as shown in Figures 8 and 9. This crosscorrelation procedure provides two important parameters: (1) a correlation time shift (ΔT) for each azimuth-dependent wavelet arrival that is based on an optimized reference wavelet and (2) a normalized correlation coefficient that can be used as a reliability factor to judge the confidence of each estimated ΔT time delay. The sign convention of crosscorrelation is such that the least-negative time shift in the crosscorrelation output corresponds to the polarization direction of the fast-S-mode (which is also the SHmax azimuth) and the most-positive time shift corresponds to the polarization direction of the slow-S-mode (which is the SHmin azimuth).

Examples of real SV-P data traces extracted from four adjacent image bins in the 3D survey are displayed in Figure 11. Visual inspection of the targeted Bass Islands reflections at 700 ms confirms that downgoing SV illumination wavelets that travel in different azimuth directions to reach an image bin create SV-P reflections that have azimuth-dependent arrival times. The Bass Islands Formation is at a depth of 3500 ft, which is one of three targeted depths where fast-SVP and slow-SVP modes were analyzed across this Michigan Basin prospect. These azimuth-dependent SV-P arrival times provide positive proof that SHmax azimuth and SHmin azimuth effects are embedded in these 3D SV-P data. The data in Figure 11 also illustrate typical noise backgrounds and wavelet irregularities that are embedded in real data, Bass Islands reflection traces across the 3D image area.

The Bass Islands SV-P reflection at 700 ms in Figure 11 is a good example of azimuth-dependent SV-P arrival times at a stacking bin. Visual examination of the four, 6-trace groups of SV-P traces on the left side of Figure 11 shows that the reflection wavelet that is embedded in the third trace from the left in each of these trace-gather panels has the earliest arrival time. This consistent SV-P traveltime behavior for these four sequential stacking bins implies that the SHmax azimuth in this small stacking-bin area of the SV-P image space is oriented approximately 60° or 70° clockwise from the north. In the shallower SV-P reflections at 600 ms, it is difficult to decide whether the SV-P wavelet in the third trace, or in the fourth trace, arrives earliest because two interfering wavelets create complex-shaped wavelets that make it difficult to define accurate arrival times. This type of wavelet interference caused our software-based selection of the SV-P first-arrival time to make inaccurate estimates of SHmax azimuths at some bins. Thus, we decided to determine estimates of the SHmax azimuth at thousands of stacking bins, and we present our results in the form of histogram plots that would reveal the most common prediction.

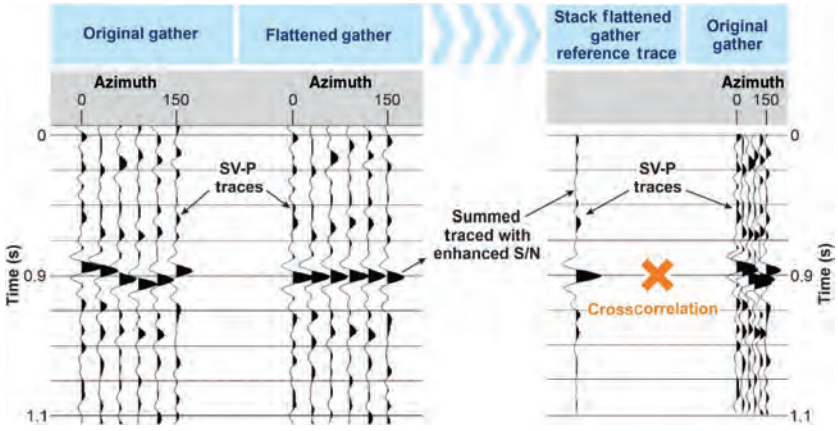

Figure 9. (Left) SV-P model traces from Figure 8. (Center) All six SV-P reflections are shifted to a constant arrival time so they can be summed to enhance the signal-to-noise ratio of the wavelet that images a targeted interface. (Right) The summed trace is then crosscorrelated with the original data traces to obtain a more accurate measure of the differences in the arrival times of each reflection wavelet. The crosscorrelation coefficients created in this procedure also provide numerical measures that indicate the consistency of wavelet shapes and allow "accept" or "reject" decisions to be made.

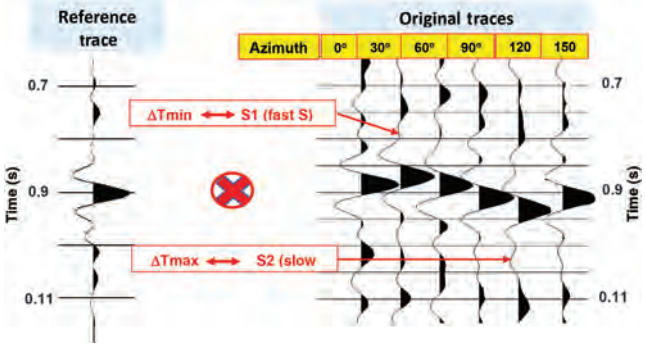

Figure 10. The crosscorrelation procedure used at each SV-P stacking bin to estimate the azimuth-dependent arrival times of the SV-P reflection wavelets from a targeted interface. The reference wavelet on the left is a summed wavelet such as that illustrated in Figure 9. The six traces on the right are crosscorrelations between this reference wavelet and the six azimuth-dependent SV-P reflection wavelets that are placed in a stacking bin by the PSTM imaging procedures. The fast-S azimuth is 30° in this example, not zero degrees as in the models in Figures 8 and 9.

DOI:10.1190/INT-2020-0226.1

Mapping azimuth-dependent SV-P velocities

The numerical trace-correlation methodology described in the preceding section was applied at SV-P stacking bins across the entire 24 mi^2 (61 km^2) 3D seismic area that we investigated. At each stacking bin, analyses were done for SV-P reflections associated with three key stratigraphic units — the Bass Islands, Niagaran (A2 carbonate), and St. Peter. These formations were located at depths of approximately 3500, 5500, and 7500 ft, respectively. Thus, we go a step beyond what, to our knowledge, previous determinations of SHmax and SHmin azimuths have done with any S-mode data; i.e., we estimated SHmax at 98,000 stacking bins at three different depth levels. Thus, we present the results of almost 300,000 estimates of SHmax.

The crosscorrelation procedure illustrated in Figure 10 was invaluable in constructing the maps of the SHmax azimuths in Figure 12. The magnitude of the crosscorrelation coefficient associated with each trace in a six-trace set at a stacking bin (such as the data in Figure 11) was used as a reliability factor to decide if the arrival time of an SV-P reflection wavelet created in a stacking bin should be accepted or rejected. The population and spatial distribution of acceptable and not acceptable SV-P reflection wavelets varied, depending on the cutoff level used to define "rejected" for a crosscorrelation value. A crosscorrelation value of 0.5 (or greater) between an averaged SV-P wavelet at a stacking bin and individual SV-P wavelets at that same stacking bin was used to decide whether to "keep" the estimate of the SHmax azimuth at that bin. This automated procedure created the color maps in Figure 12. This procedure also resulted in a different number of stacking bins and in stacking bins located at different x–y coordinates, contributing to each histogram in Figure 12.

This area of the Michigan Basin is covered with a glacial till surface layer that is approximately 1000 ft (300 m) thick. The internal fabric of this thick glacial till changes abruptly over short distances, as one would expect a giant bulldozer, like a large moving glacier, to create as it pushes material across Canada and into the Michigan Basin. As a result of its internal complexity, this glacial till layer is known as one of the most challenging locations to determine P-wave statics. The determination of S-wave statics at the source stations where downgoing illuminating SV wavefields are generated is even more challenging than determining the P-wave statics. Inaccurate estimates of the S-wave statics at some source stations certainly had some effect on interpreting SV-P arrival times in low-fold, narrow-corridor data.

Considering these concerns, the estimates of the SHmax azimuth shown in Figure 12 are quite encouraging. Each histogram is based on several tens of thousands of estimations distributed across the SV-P image space. One way to obtain a feel for the number of normal-sized stacking bins that are inside the SV-P image space is to examine the maps on the left side of Figure 12. Each square in the background grid of these maps is an area of (50 stacking bins) × (50 stacking bins). The SV-P image area spans approximately 24 mi^2 (approximately 61 km^2). There are slightly more than 98,000 stacking bins across this SV-P image space.

The estimates of the SHmax azimuth displayed in Figure 12 are evidence of the robustness of using arrival times of SV-P reflection wavelets to define the fast-S azimuth (i.e., the SHmax azimuth). Consistent estimates that SHmax azimuth is approximately 65° (±15°) clockwise from the north were obtained at formation boundaries at three different depths (3500, 5500, and 7500 ft). At each of these depths, estimates of the SHmax azimuth were based on the analyses of azimuth-dependent SV-P arrival times at several tens of thousands of stacking bins. The crosscorrelation procedure that we used to determine the SV-P reflection quality at each stacking bin means that a stacking bin that contributes to the histogram plot at one horizon may not qualify to contribute to a histogram plot at a

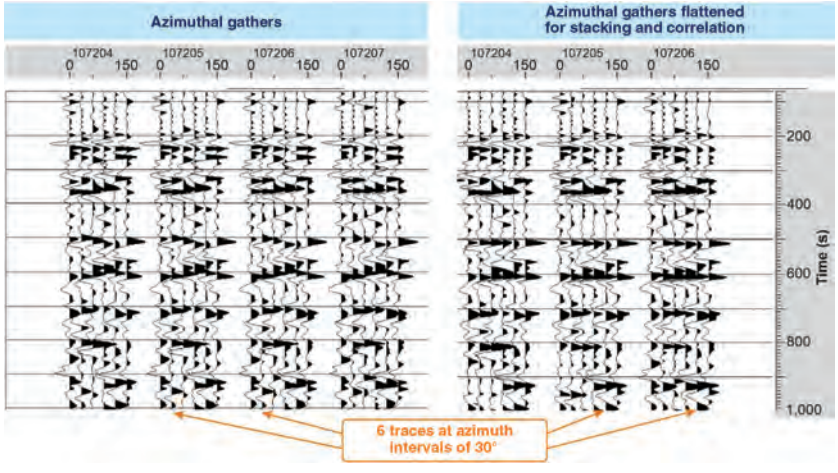

Figure 11. Real SV-P data traces that illustrate the complex shapes of the azimuth-dependent SV-P reflection wavelets that arrive at four adjacent SV-P stacking bins. The numbers at the top of each trace indicate the azimuth direction of the narrow corridor that encompassed the source-receiver pairs that created the data trace. The Bass Islands reflections are located at 700 ms. The inconsistent waveshapes of these reflections are the reason why a wavelet-summing and crosscorrelation procedure was used to create a best estimate of the arrival time of each SV-P imaging wavelet at each stacking bin. (Left) Visual inspection of these four 6-trace groups shows that the earliest arriving Bass Islands reflection always occurs in the third trace from the left, which is a stacked trace created in a 30° corridor that is oriented 60° clockwise from the north. (Right) Flattened reflections at 600 and 700 ms illustrate the types of wavelet interferences that exist in some stacking bins. The six-trace gather at bin 107207 (left) is not repeated as a flattened-reflection version (right).

different horizon. It is correct to state that accept/reject analyses were made at approximately 98,000 stacking bins across each of the three targeted horizons to create the three histograms displayed in Figure 12.

Comparison of the seismic prediction of SHmax with ground truth information

Fortunately, local ground-truth measurements are available to determine if these azimuth-dependent arrival times of SV-P reflections are providing reliable estimates of the SHmax azimuth. This ground-truth information is described in a report prepared by others in 2019 for the U.S. Department of Energy (Battelle, 2019). The local stress-azimuth measurements assembled by these earlier investigators are summarized in Figure 13.

- Figure 13a: Drilling-induced fractures were analyzed in a well drilled inside the seismic image space. Only six such fractures were found. Investigators concluded that these fractures were less reliable than fractures created by minifrac tests but noted that two of these drilling fractures were oriented in an azimuth of 58°.
- Figure 13b: Four minifrac tests were performed in this same well inside the seismic survey area. These tests indicated that the SHmax azimuth was either 54° or 62°. Both predictions are within the SHmax azimuth range predicted by the SV-P reflection arrival times (Figure 12). A third SHmax direction of 33° was also inferred, but this measurement could be a shear fracture, not a required extensional fracture. Shear fractures will be oriented away from extensional fractures (i.e., SHmax azimuth) by approximately 30°.
- Figure 13c: A locally interpreted fault, based on well-log analyses, was oriented at an azimuth of 65°. Fault evidence of the SHmax azimuth should always be honored unless there is compelling evidence that the SHmax azimuth has been altered by later regional stress dynamics. No information was provided in this earlier study about the second fault oriented at 5° that is shown in this data panel.

Thus, there is a rather good agreement between the three SV-P traveltime predictions of the SHmax azimuth in Figure 12 and local ground-truth data. We conclude that determining the SHmax (i.e., fast-S) azimuth by measuring the SV-P reflection arrival times in rotating narrow-azimuth gathers of SV-P traces is a reliable and robust data analysis method. This new S-wave physics will be an important principle to insert into the geophysical literature.

It should be noted that if legacy P-source data are recorded by 3C geophones, then those data can be used to create not only a traditional P-SV image but also an SV-P image and an S-S image. An elegant method for creating S-S information from 3C P-source data, which involves combining P-P data with P-SV data, has been proposed by Grechka and Tsvankin (2002). We wish to point out that our study presents a second option for creating S-S images from 3C P-source data. This second option would use the same downgoing direct-S P-source wavefield that we have used, but it would then use upgoing S reflections that are recorded by horizon-

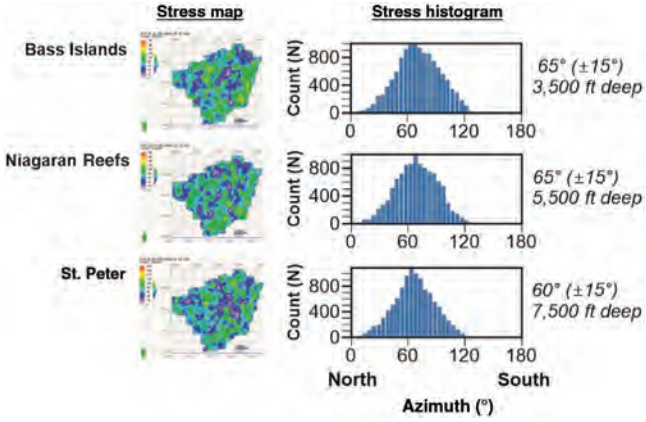

Figure 12. Estimates of the SHmax azimuth (fast-S azimuth) at three different formation depths (3500, 5500, and 7500 ft) across the 3D seismic survey area. (Left) Color maps at each depth across the 24 mi^2 (61 km^2) 3D survey area that show estimates of the SHmax azimuth. We found it difficult to reach quantitative conclusions about the SHmax azimuth by map examination, so these maps are shown in a small scale just to indicate the area that was analyzed at each depth. (Center) The histogram plots of estimates of the SHmax azimuth made at all stacking bins at each formation depth were a convenient way to display our data analyses. The stacking bin dimensions were 82.5 × 82.5 ft (25 × 25 m), and 98,000 bins were analyzed at each depth. Each histogram spike is the average SHmax value inside a (3 bin) × (3 bin) area that moves across the image space. (Right) This information states the mean and standard deviation values of each SHmax-azimuth histogram. The important information about SHmax azimuth contained in the maps on the left is well expressed by the statistical parameters written on the far right.

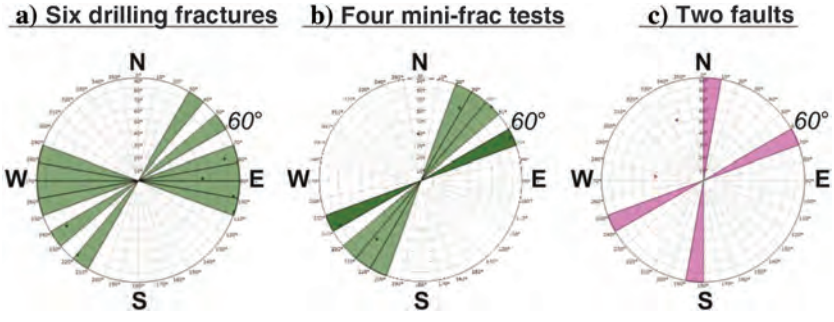

Figure 13. Nonseismic, ground-truth measurements of the SHmax azimuth at the 3D seismic survey area. (a) Six drilling-induced fractures. (b) Four minifrac tests. (c) Two faults interpreted from local well-log analyses. Comments are provided in the text. The data are described in a report by Battelle (2019).

DOI:10.1190/INT-2020-0226.1

tal geophones, rather than using upgoing converted-P reflections that are recorded by vertical geophones.

Our concept of determining the SHmax azimuth by measuring azimuth-dependent arrival times of the SV-P reflections is a wave-propagation physics that has never been demonstrated until now, to our knowledge. This new S-wave physics, when coupled with the data examples published in the papers cited in the reference list, shows the full equivalence between SV-P data and P-SV data. For all who practice seismic reflection seismology, this paper should provide evidence of the value of the downgoing direct-S wavefields produced by P-sources.

Conclusion

Traditional P-wave seismic sources produce direct-S illuminating wavefields that can be effective for illuminating deep rocks just like the direct-P wavefields that are produced by these sources. Reflection seismologists have used the direct-P wavefields produced by vertical vibrators and buried explosives for decades. In contrast, they have ignored the companion direct-S illuminating wavefield generated by these sources. This latter statement can be verified by searching the geophysical literature to find examples of S-mode data generated by a P-source and recorded by vertical geophones. We cannot find such examples.

The direct S-mode produced by P-sources allows S-mode reflection seismology to be practiced with seismic data generated by traditional P-sources and recorded with only vertical geophones. This new approach to S-wave reflection seismology can be achieved by using SV-P reflections that are intertwined with P-P reflections in vertical-geophone data. An SV-P mode is created when a downgoing direct-SV illuminating wavefield produced by a P-source converts to upgoing P reflections at rock interfaces. These upgoing converted-P reflections are recorded by vertical geophones just as are the upgoing direct-P reflections created by a downgoing illuminating P wavefield.

The 3D seismic data used in this research were legacy data. Our work shows that others can also retrieve P-source, vertical-geophone data from legacy-data storage and use those data to create SV-P images of deep rocks. S-wave reflection seismology can thus be practiced without expending any funds to acquire new seismic data. If there are legacy data generated by a P-source and recorded by 3C geophones, then those data can also be retrieved from data storage and used to create S-S images. This expansion to S-S imaging options is possible because the downgoing illuminating SV wavefield produced at P-source stations will create upgoing S reflections that will be recorded by surface-based horizontal geophones.

Our demonstration that fast-S and slow-S azimuths can be determined by analyzing azimuth-dependent arrival times of SV-P reflections should be a valuable technique for evaluating fractured-rock targets and for detecting subtle faults that are not well identified by P-wave data. Our SV-P data-processing procedure has particular appeal because it can be practiced with legacy P-source, vertical-geophone data that are already recorded and are lying dormant in data-storage facilities around the globe.

Acknowledgments

This report describes research accomplishments achieved with funding provided through Department of Energy (DOE) award no. DE-FE0031686. The purpose of this DOE funding was to develop methods that provide information about stress fields that act on deep rocks without invading the earth to acquire that information.

Data and materials availability

Seismic data associated with this research are confidential and cannot be released.

References

Al-Hawas, K., M. Ameen, M. Wahab, E. Nebrija, and C. MacBeth, 2003, Delineation of fracture anisotropy signatures in Wudayhi Field by azimuthal seismic data: The Leading Edge, **22**, 1202–1211, doi: 10.1190/1.1641372.

Battelle, 2019, Task 4 (field testing report): A non-invasive approach for elucidating the spatial distribution of in-situ stress in deep subsurface geologic formations considered for CO_2 storage: prepared by Battelle, prepared for U.S. Department of Energy National Energy Technology Laboratory, DOE Award Number DE-FE0031686.

Graul, M., 2017, AVO and interpretive processing of SV-P reflections co-existing with P-P reflections on P-wave legacy data: 87th Annual International Meeting, SEG, Expanded Abstracts, 5157–5161, doi: 10.1190/segam2017-17782672.1.

Grechka, V., and I. Tsvankin, 2002, PP + PS = SS: Geophysics, **67**, 1961–1971, doi: 10.1190/1.1527096.

Gupta, M., and B. Hardage, 2017, Improved reservoir delineation by using SV-P seismic data in Wellington field, Kansas: 87th Annual International Meeting, SEG, Expanded Abstracts, 5182–5186, doi: 10.1190/segam2017-17559574.1.

Hardage, B., R. Van Dok, M. Graul, A. Modroo, V. Smith, and M. Kelley, 2020, Task 2 Report: Extracting stress data from seismic data, a non-invasive approach for elucidating the spatial distribution of in-situ stress in deep subsurface geologic formations considered for CO_2 storage: prepared by Battelle, submitted to National Energy Technology Laboratory Technology Development and Integration Center Carbon Storage Team, DOE Award Number DE-FE0031686.

Hardage, B. A., 2011, System and method for acquisition and processing of elastic wavefield seismic data: U.S. Patent US 8,040,754 B1.

Hardage, B. A., 2012a, System and method for acquisition and processing of elastic wavefield seismic data: U.S. Patent US 8,164,979 B2.

Hardage, B. A., 2012b, Extracting SV shear data from P-wave seismic data: U.S. Patent US 8,243,548 B2.

Hardage, B. A., 2017a, Practicing S-wave reflection seismology with "P-wave" sources — Concepts, principles, and overview: 87th Annual International Meeting, SEG, Expanded Abstracts, 5152–5156, doi: 10.1190/segam2017-17256173.1.

Hardage, B. A., 2017b, Examples of SV-P images made with P-sources and vertical geophones: 87th Annual International Meeting, SEG, Expanded Abstracts, 5187–5191, doi: 10.1190/segam2017-17430569.1.

Hardage, B. A., 2017c, Real-data comparisons of direct-S modes produced by "P" sources and "gold standard" S sources: 87th Annual International Meeting, SEG, Expanded Abstracts, 2481–2485, doi: 10.1190/segam2017-17430461.1.

Hardage, B. A., 2017d, Land based S-wave reflection seismology with P-sources — Does it work?: 87th Annual International Meeting, SEG, Expanded Abstracts, 6067–6061, doi: 10.1190/segam2017-w11-04.1.

Hardage, B. A., D. Sava, and D. Wagner, 2014, SV-P — An ignored seismic mode that has great value for interpreters: Interpretation, **2**, no. 2, SE17–SE27, doi: 10.1190/INT-2013-0096.1.

Hardage, B. A., and D. Wagner, 2014a, Generating direct-S modes with simple, low-cost, widely available seismic sources: Interpretation, **2**, no. 2, SE1–SE16, doi: 10.1190/INT-2013-0095.1.

Hardage, B. A., and D. Wagner, 2014b, S-S imaging with vertical-force sources: Interpretation, **2**, no. 2. SE29–SE38, doi: 10.1190/INT-2013-0097.1.

Hardage, B. A., and D. Wagner, 2018a, Direct-SV radiation produced by land-based P-sources — Part 1: Surface sources: Interpretation, **6**, no. 3, T569–T584, doi: 10.1190/INT-2018-0046.1.

Hardage, B. A., and D. Wagner, 2018b, Direct-SV radiation produced by land-based P-sources — Part 2: Buried explosives: Interpretation, **6**, no. 3, T585–T599, doi: 10.1190/INT-2018-0047.1.

Karr, B., 2017, SV-P imaging compared to P-SV imaging — Analysis of statics and velocities required to create an SV-P image: 87th Annual International Meeting, SEG, Expanded Abstracts, 5177–5181, doi: 10.1190/segam2017-17728712.1.

Li, Y., and B. A. Hardage, 2015, SV-P extraction and imaging for far-offset vertical seismic profile data: Interpretation, **3**, no. 3, SW27–SW35, doi: 10.1190/INT-2015-0002.1.

Li, Y., D. Wang, S. Shi, and X. Cui, 2017, Gas reservoir characterization using SV-P converted wave mode — A case study from western China: 87th Annual International Meeting, SEG, Expanded Abstracts, 5172–5176, doi: 10.1190/segam2017-17726552.1.

Lynn, H. B., 2004a, The winds of change: Anisotropic rocks — Their preferred direction of fluid flow and their associated seismic signatures — Part 1: The Leading Edge, **23**, 1156–1162, doi: 10.1190/1.1825938.

Lynn, H. B., 2004b, The winds of change: Anisotropic rocks — Their preferred direction of fluid flow and their associated seismic signatures — Part 2: The Leading Edge, **23**, 1258–1268, doi: 10.1190/leedff.23.1258_1.

Smith, R. L., and J. P. McGarrity, 2001, Cracking the fractures — Seismic anisotropy in an offshore reservoir: The Leading Edge, **20**, 18–26, doi: 10.1190/1.1438870.

Wagner, D., and B. A. Hardage, 2017, Using finite-difference modeling to understand direct-SV illumination produced by P-sources: 87th Annual International Meeting, SEG, Expanded Abstracts, 5167–5171, doi: 10.1190/segam2017-17661718.1.

Xu, S., and M. S. King, 1989, Shear wave birefringence and directional permeability in fractured rock: Scientific Drilling, **1**, 27–33.

Biographies and photographs of the authors are not available.